SURFACE AND INTERFACE ANALYSIS OF PHOTOVOLTAIC DEVICES

L.L. Kazmerski
Solar Energy Research Institute
Golden, Colorado 80401, U.S.A.

Interface chemistry can control the performance and operational lifetime of solar cells, especially thin-film, polycrystalline devices. The composition and elemental integrity of device surfaces, internal junctions, layer and defect interfaces can be related to and dominate the electro-optical characteristics of the materials/devices. This paper examines the compositional properties of external and internal surfaces in polycrystalline solar cells, utilizing high-resolution, complementary surface analysis techniques. The electronic properties of these same regions are evaluated using microelectrical characterization methods. Cell performance, in turn, is explained in terms of these relationships. Specifically, two solar cell types are used as examples: (1) the polycrystalline Si homojunction; and, (2) the (CdZn)S/$CuInSe_2$ heterojunction. Throughout these investigations of photovoltaic devices, the limitations and strengths of the surface and electrical microanalyses techniques are emphasized and discussed.

Solar Cells, Surface Analysis, Thin Films

1. Introduction

Interface chemistry can control the performance and operational lifetime of photovoltaic devices, especially thin-film, polycrystalline cells.[1-3] The composition and impurity integrity of device surfaces, internal junctions, layer and defect interfaces can be related to, as well as dominate, the electro-optical characteristics of the materials and solar cells. Although relatively simple in

structure and operation when compared to a variety of more complex devices found in current semiconductor electronics, the solar cell does have a number of important and inherent interfaces that control its operation. Fig. 1 presents a generic representation of a solar

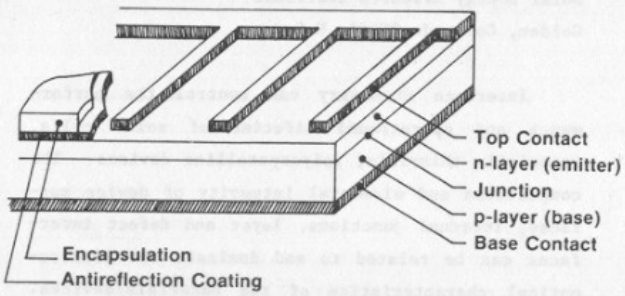

Fig. 1: Generic Solar Cell

cell. The major device interfaces include the antireflection coating/semiconductor, the upper contact (grid, finger or transparent conducting film) to the top semiconductor layer, the semiconductor-semiconductor junction, and the metallic back contact/semiconductor interface. In a polycrystalline solar cell, these material interfaces are complicated by internal ones--primarily grain boundaries. These intercrystalline defects can be sites for recombination of minority and majority carriers (causing loss of open-circuit voltage and short-circuit current), for shunting paths due to low conductance of these regions, and for enhanced diffusion of impurities or other elemental species through the thin layers. The identification of compositional problems at any of these device interfaces is important in both preserving and evolving the performance of these energy-conversion devices.

In this paper, complementary, high-resolution scanning Auger electron spectroscopy (AES), electron energy loss spectroscopy (EELS), X-ray photoelectron spectroscopy (XPS), and secondary ion mass spectrometry (SIMS) are used to investigate the compositional properties of external and internal surfaces in polycrystalline solar cells. The electrical properties of these same regions are evaluated using microanalytical techniques, including electron beam induced current (EBIC), and are correlated directly with the surface analysis

results. Device performance (i.e., conversion efficiency, dark/light J-V characteristics) is, in turn, explained in terms of these relationships. Two solar cell types are used as examples: (1) polycrystalline Si homojunction; and, (2) thin-film (CdZn)S/$CuInSe_2$ heterojunction. For the former, the emphasis is placed upon grain boundary problems. AES and SIMS are used to map impurities localized on these intergrain regions. Electrical properties and minority carrier lifetimes of clean and intentionally-doped Si grain boundaries are presented. The critical effects of temperature-activated oxygen segregation on the electrical activation of these intergrain regions are identified. For the latter, heterojunction device, correlations between cell processing and cell structure are identified using surface analysis techniques. The initial formation of CdS on the Cu-ternary semiconductor is investigated using angular-resolved XPS and EELS. Finally, the effects of the critical post-fabrication oxygen heat-treatment are discussed in terms of ternary type-conversion and heterojunction activation. In these examples, the limitations and strengths of the microanalysis (compositional and electrical) techniques are presented for solar cell and semiconductor device applications.

2. Methods of Analysis

Each of the surface analytical techniques can be described simply in terms of the "input" probe and the measured "output" parameter. These are summarized, along with some important features of each method, in Table 1. The methods are complementary in the information they provide or in the sensitivity they possess. Each is surface-sensitive, since only the topmost 3-50 Å of the material is analyzed. This is due either to the escape depth of emitted charged carriers (AES, XPS) or the removal and analysis of individual atomic layers (SIMS). Auger electron spectroscopy involves having one electron from a less tightly bound orbital fill the vacancy, while a second electron (called the Auger electron) is ejected into the continuum with an energy equal to the difference in the total energies of the initial and final states. Since the AES process requires at least two energy states and three electrons, it cannot detect hydrogen. Its elemental sensitivity is limited to about 0.1 at-%.

Table I Summary of Selected Surface Analysis Techniques

	AES	EELS	SIMS	XPS	UPS
Probe	electron	electron	ion (+, -)	x-ray	ultraviolet
Detected Species	electron	electron	ion (+, -)	electron	electron
Spatial Resolution	~300 Å	~300 Å	<1 μm	10^2 - 10^3 μm	~10^3 μm
Depth Resolution	5 - 50 Å	5 - 50 Å	≥ 3 Å	5 - 50 Å	5 - 50 Å
Detection Sensitivity	0.1 at-%	0.1 at-%	<0.001 at-%	0.1 at-%	0.1 at-%

However, since the input probe is composed of electrons, very high spatial resolution (<300 Å) can be obtained. This is especially useful when used in a scanning mode to map impurity concentrations on a surface. Electron energy loss spectroscopy involves single particle excitations from filled to empty electronic states by bombarding the surface with low-energy (i.e., less than 500 keV) electrons. The method is similar to AES, and can be performed in such systems if the analyzer has sufficient energy discrimination. Secondary ion mass spectrometry involves the mass analysis of secondary (positive and negative) ions emitted from a solid as a result of ion bombardment or ion etching. SIMS can detect hydrogen, and is several orders of magnitude more sensitive to trace elements than AES. Since it is more difficult to focus ion beams to small diameters, the method does not have the spatial resolution of AES. However, modern instruments are now able to map impurity distributions to the submicron level. SIMS can be used to detect molecular fragments and isotopes, but is difficult to quantify. X-ray photoelectron spectroscopy energy analyzes photoelectrons emitted from a solid surface as a result of X-ray excitation. This core level analysis technique can identify composition and chemical bonding from shifts in the peak positions in the binding energy spectra. Since the input-probe is relatively non-destructive, it is the least damaging of the surface analysis methods. It has the same elemental sensitivity as AES, but can provide more reliable quantitative information. It lacks the spatial resolution of SIMS and AES.

Electron-beam induced current techniques provide information on the electrical activity of electronic junctions in a material.[4] These junctions may be purposely-placed, as in a diode, or the result

of the depletion of carriers around a crystalline defect. In this technique, the current induced by an incident electron beam is spatially resolved. Changes in such induced current are indicative of regions of current collection or loss in a material.

All the compositional-related techniques can provide elemental-depth information. AES and XPS can be combined with ion etching. SIMS has this feature inherent to the analysis method. First principle calculations can be used to obtain semiquantative information on composition for any of these techniques. However, the more precise method of quantification involves the use of standards, chemically-close to that being evaluated. A variety of instrumentation is available for these surface analysis operations. The purpose of this section is to summarize the methods as used in this paper. Further information on the techniques and the instrumentation can be gained from several excellent review articles and texts currently available.[5-8].

The compositional and chemical determination were performed primarily with surface analysis equipment. These include: (1) Perkin-Elmer/Physical Electronics model 595 Multiprobe, having better than 500 Å AES resolution, complementary SIMS, EBIC and EDS capabilities; (2) Perkin-Elmer/Physical Electronics model 590 and 595 Scanning Auger microprobe, with 1500 Å resolution respectively, complementary SIMS and EBIC; (3) Perkin-Elmer/Physical Electronics model 550 XPS/AES system, with EELS, SIMS and EBIC; and, (4) CAMECA IMF-3f ion microprobe, with Ce and O ion sources. AES measurements were typically taken under low current (~ 20 nA) conditions, using the pulse counting detection mode. XPS data were taken with a 10 kV (40 mA) X-ray source, configured with a Mg anode, utilizing a double pass cylindrical mirror analyzer 10 eV pass energy was used for high resolution. The EELS was done using the double-pass analyzer with an incident energy of 100 eV. A 0.5 eV modulation energy was used in these studies. Electron beam induced current studies were performed in-situ, as well as in a JEOL 35C SEM, equipped with digital imaging capabilities. Minority carrier lifetimes were determined using a spatially resolved surface photovoltage method.[11] Resolution was typically 15 μm , using a microfocussing stage. Measurements for the

Si samples were taken over the range $0.88 < \lambda < 1.0$ μm, with better than a 5% reproducibility.

3. Grain Boundaries in Silicon

Polycrystalline semiconductors have become important entities in the electronics industry, with applications ranging from passive micron-size interconnects to active, cm-size solar cells. Silicon is a major semiconductor for these applications, and the control and understanding of the properties of the grain boundaries in this polycrystalline material is of fundamental importance. Surface analysis has provided the first direct means of detecting impurities at intergrain regions, showing their localization and concentration levels.

3.1 Segregation of Impurities

The direct evidence for the segregation of impurities to grain boundaries in polycrystalline Si has been reported.[9-11] Since grain boundaries lie essentially perpendicular to the available surface, they offer a low-profile for analysis, even by current high-resolution probes. In-situ, ultrahigh vacuum fracturing has been demonstrated as a successful method to expose these internal surfaces, providing larger areas for analysis and mimimizing potential contamination from absorbed chemical species.[9] The method also provides for side-by-side analysis of grain and grain boundary regions under identical conditions for comparison. Fig. 2 presents such data utilizing AES survey scans. In this case, the boundary region is observed to contain several detectable impurity species (C, O, Fe, F, Al), not seen in the bulk of the grain itself. In fact, the localization of these impurities on the grain boundary surface can be illustrated by tuning the spectrometer to each of these impurities and mapping their positions on the grain boundary surface, as shown in Fig. 3.

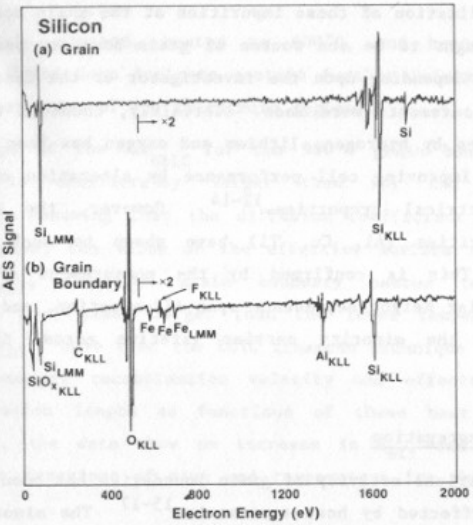

Fig. 2: AES survey scans of (a) adjacent grain, and (b) grain boundary in fractured polycrytalline silicon (Ep = 2kV, Ip = 30 nA).

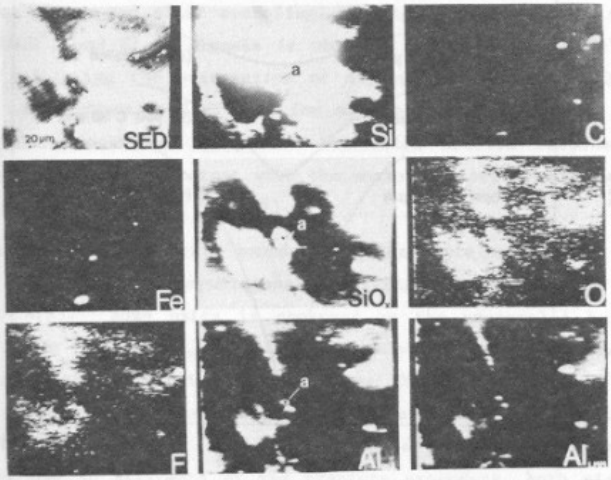

Fig. 3: Scanning AES maps of grain boudary exposed in UHV by fracturing and showing localization of impurities. SED image shows topography (from ref. 11)

The localization of these impurities at the grain boundaries was initially thought to be the source of grain boundary passivation or activation — depending upon the investigator or the condition under which the measurements were made. Certainly, chemical treatment of grain boundries by hydrogen, lithium and oxygen has been shown to be effective in improving cell performance by alteration of the grain boundary electrical properties.[12-14] However, the addition of various impurities (Al, Cu, Ti) have shown no such passivation effects.[11] This is confirmed by the measurement of the grain boundary barrier height dependence upon illumination, and the spatial variation of the minority carrier lifetime across the boundary region.[11]

3.2 Oxygen Segregation

The electrical activity of grain boundaries has been reported to be strongly affected by heat treatments.[15-17] The minority carrier collection can be seen to increase significantly at higher annealing temperatures. Fig. 4 shows individual EBIC linescans across a grain

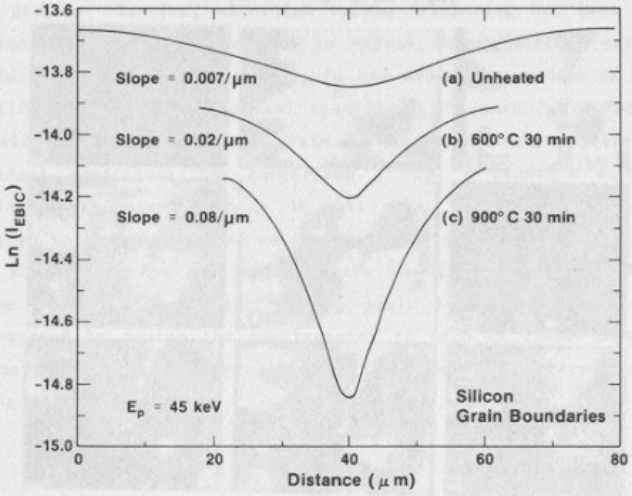

Fig. 4: EBIC linescans across (a) unannealed: (b) heat-treated, 600°C, 30 min; and (c) heat-treated, 900°C, 30 min, grain boundaries in silicon. Increase in electrical activity at these regions is observed.

boundary under unheated, heated to 600°C, and heated to 900°C processing. These data indicate contain further information on the electrical properties of the intergrain regions.

The slope of the $\lambda n I_{EBIC}$ for the 900°C grain boundary anneal ($\sim 0.08 \mu m^{-1}$) is considerably larger than for the 600°C case ($\sim 0.02 \mu m^{-1}$). Assuming that the diffusion coefficient is the same for both samples, the value of the effective surface recombination velocity, S_{eff}, for the grain boundary heated to 900°C is approximately four times larger than the lower temperature case. Russell, et al.[18] have used the EBIC linescan technique to determine the grain boundary recombination velocity and effective minority carrier diffusion length as functions of these heat treatments. Statistically, the data show an increase in S_{eff} and decrease in L_{eff}, both as functions of time and temperature for these Si grain boundaries.

The activation of these grain boundary regions has been attributed to either the movement of impurities to the grain boundary, or away from it. Fig. 5 presents SIMS data taken on fractured grain regions, before and after annealing. A significant increase in the $SiO^{\pm}$, $SiOH^{+}$, and Si_2O^{+} signals is observed after heating (900°C, 30 min.), indicating the segregation of oxygen to these internal surfaces. Also shown in SIMS data for an annealed Al-containing grain boundary. Almost no change in the oxide species response was observed. This is consistent with the measured electrical properties of such grain boundaries (Fig. 4).

In addition, the grain boundary surfaces were examined by fracturing and SIMS depth-compositional profiling. The results are shown in Fig. 6(a). Some oxide is observed on the unannealed boundary surface. By comparison, however, a more pronounced oxide layer is measured on the annealed surface. Since the data were taken under identical conditions, the relative depths and Si-O coverage can be qualitatively compared. In order to ensure that those differences were not due to artifacts of the fracture procedure, both sides of the fractured surface were examined. This painstaking procedure resulted in the two sets of data shown on each depth profile. For

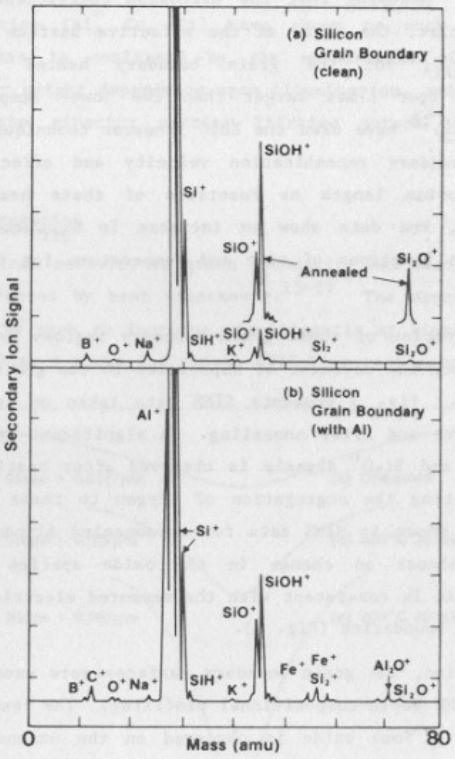

Fig. 5: SIMS data for heat-treated and unannealed grain boundaries. (a) Clean region (no intentional impurities added), showing increase in SiO^+ with 900°C, 30 min heat treatment.

this particular grain boundary, a minority carrier lifetime scan was also recorded (before fracture) in Fig. 6(b). The annealed grain

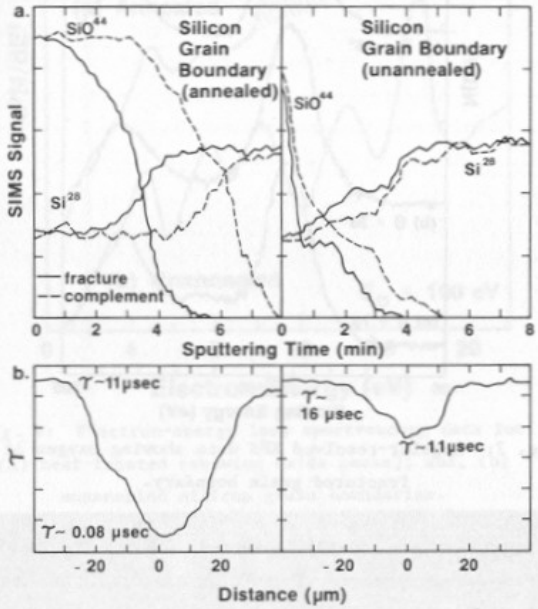

Fig. 6: Si grain boundary: (a) SIMS depth profile for annealed and unannealed cases. Date for both sides of fracture are presented. (b) Minority carrier lifetime linescan for corresponding regions (from ref. 9).

boundary has a lower τ , which complements both the EBIC and the SIMS data. Further evidence of the oxide present at this grain boundary is presented by the XPS and EELS data of Figs. 7 and 8. Figure 7 presents angle-resolved XPS data for both a fractured, unheated grain boundary, and one heated at 900°C. The Si-2p signals are shown as a function of the effective analyzer acceptance angle, θ. EELS data, shown in Fig. 8, also indicates the differences in the unheat-treated and heat-treated grain boundaries. The loss peaks associated with

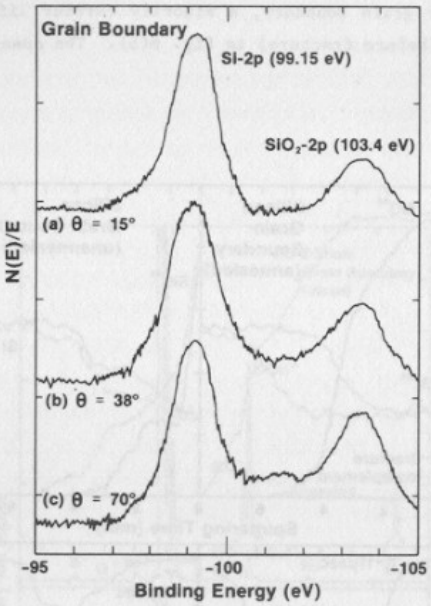

Fig. 7: Angular-resolved XPS data showing oxygen at fractured grain boundary.

the oxide species are easily observed (shaded regions) in the annealed grain boundary case. Therefore, the origin of the enhanced grain boundary electrical activity in heat-treated polycrystalline Si is due to the segregation of the oxygen to the intercrystalline boundary regions. A final illustration of this effect is shown in Fig. 9, which presents a SIMS map of oxygen on a polycrystalline Si sample annealed at 900°C. The accumulation of oxygen at the boundary region (intersection of the grain boundary with the wafer surface) is readily apparent. It must be stressed that not all grain boundaries exhibit the enhancement in electrical activity after annealing. This may well be due to other impurity effects or to crystallographic properties of the grains and grain boundaries.

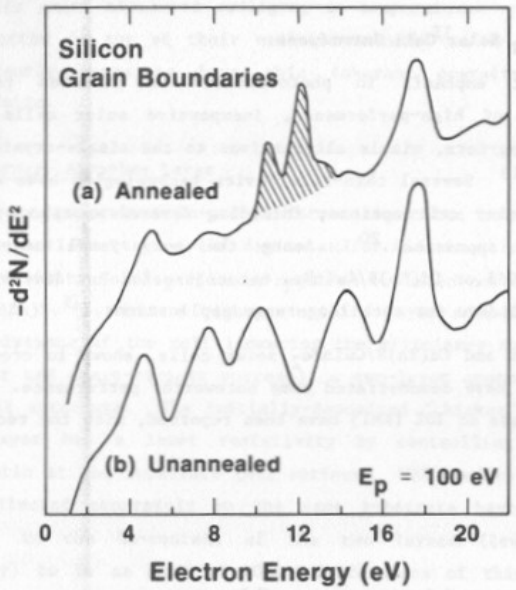

Fig. 8: Electron-energy loss spectroscopy data for (a) heat-treated (showing oxide peaks); and, (b) unannealed silicon grain boundaries.

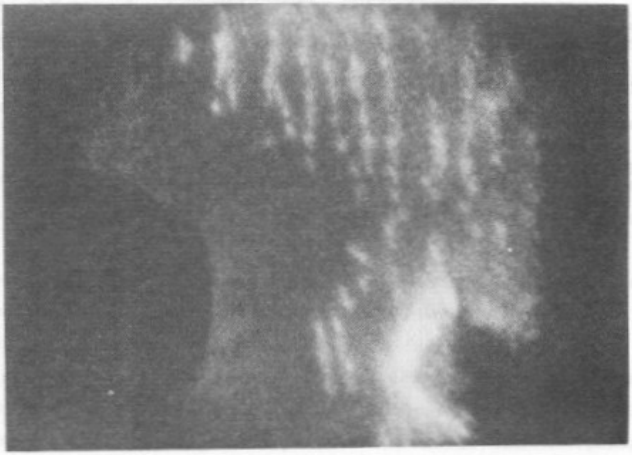

Fig. 9: SIMS oxygen map directly indicating oxygen segregation to grain boundary.

4. $CuInSe_2$ Solar Cell Interfaces

Current emphasis in photovoltaics is directed toward the development of high-performance, inexpensive solar cells that can serve as long-term, viable alternatives to the single-crystal silicon technology.[19] Several thin-film device technologies have emerged as potential solar cell options, including several amorphous and polycrystalline approaches.[20] Among the polycrystalline, thin-film cells, the CdS or $Cd(Zn)S/CuInSe_2$ heterojunction has developed into a leading candidate for such long-range applications.

The CdS and $Cd(Zn)S/CuInSe_2$ solar cells, shown in cross-section in Fig. 10, have demonstrated some noteworthy performance. Efficiencies in excess of 10% (AM1) have been reported, with the recently

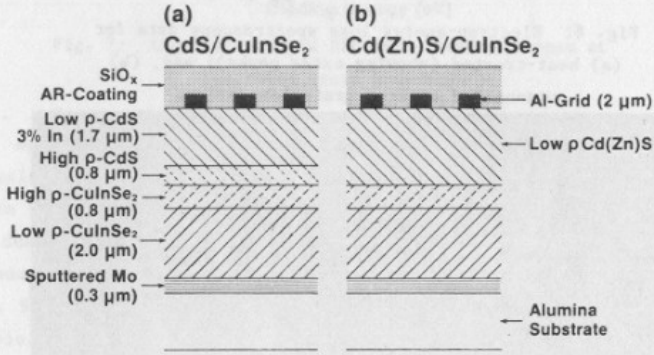

Fig. 10: Solar cell cross-sections: (a) $CdS/CuInSe_2$ heterojunction: (b) $(CdZn)S/CuInSe_2$ heterojunction.

measured 10.3% value the highest for any thin-film cell to date. The device is a true thin-film configuration, with the total device thickness of the order of 7-8 μm (see Fig. 10). Finally, these heterostructures have given evidence of extraordinary stability. Unencapsulated devices have been operated for more than 7500 hours,

continuously under simulated sunlight, at temperatures ~ 60°C, with no degradation in any of their cell parameters.[21] No other solar cell currently seems to have this inherent operating lifetime characteristic.

4.1 Cu-Ternary Absorber Layer

In order to prevent Cu-nodule formation at the heterointerface (and subsequent shorting of the device and/or low shunt resistances), a high-resistivity $CuInSe_2$ film is required to be in contact with the CdS or (CdZn)S.[21] Since a high-resistivity layer adds to the total series resistance of the cell (lowering the efficiency through lower fill-factor and short-circuit current), a two-layer approach is used in the cell structure. The initially-deposited "thicker" (~ 2.5 μm) $CuInSe_2$ layer has a lower resistivity by controlling the Cu:In arrival ratio at the substrate (Mo) surface. EDS studies of the two layers collected separately on the same substrate have shown the difference in the Cu-content of the two layers (low and high resistivity) to be as much as 10%. Differences of this magnitude would have obvious implications for preservation of the assumed chalcopyrite crystal structure of this Cu-ternary in the cell.[22] In order to determine if such compositional differences do result in the bilayer $CuInSe_2$ cell structure, AES studies were performed on the ternary film in fabricated devices. The 0.1 at.-% resolution of the AES method is certainly adequate to find compositional differences expected to several orders of magnitude larger than this limit.

Depth-compositional profiles of these thin-film structures, such as that presented in Fig. 11, indicate no difference in the Cu (or In and Se) composition through the two layers, within the resolution limits of the technique.[24] In fact, no differences have been detected in films produced by several different research groups using the same Boeing two-layer scheme. In order to make certain that the constant composition was not due to differential sputtering and mixing of the layers, the compositional analysis was performed on the cell cross-section. In this technique, the sample is fractured, and AES compositional mapping is used to produce and elemental linescan

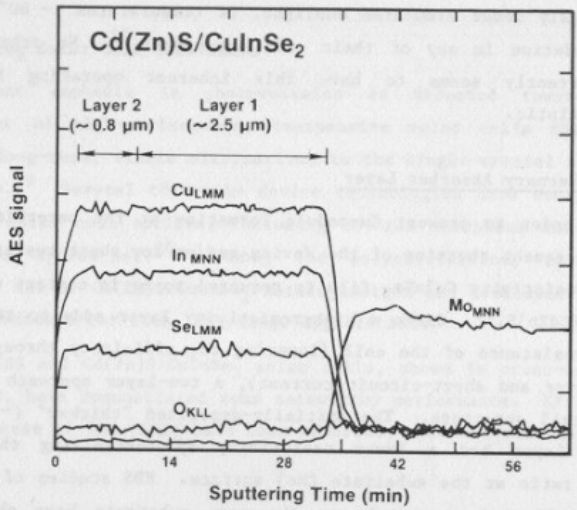

Fig. 11: AES depth-compositional profile showing constant elemental composition across $CuInSe_2$ bilayer absorber. (Ep - 5kV, Ip = 10 nA, Ar-sputtering.)

across the exposed device cross-section. The cross-section is presented in Fig. 12, a secondary electron micrograph. The various layers of the heterojunction cell are easily observable. The various device regions (i.e., CdS, $CuInSe_2$, Mo) are checked for elemental composition using AES. The cross-sectional linescans of the Cu, In, and Se Auger signals are presented in Fig. 12. These have been corrected for the sample's topographical features that affect the collection of the Auger electrons.[23] These data, which are completely reproducible across the exposed region, complement the depth-compositional studies, showing no large detectable differences in Cu (or In and Se) between the two layers. The interface regions appear to be less abrupt than they actually are (compare Figs. 11 and 12) due to the integrating effect of the 1 μm AES beam as it scans the region. Additional evidence for the apparent constant composition across the two layers is presented in the SIMS data of Fig. 13.

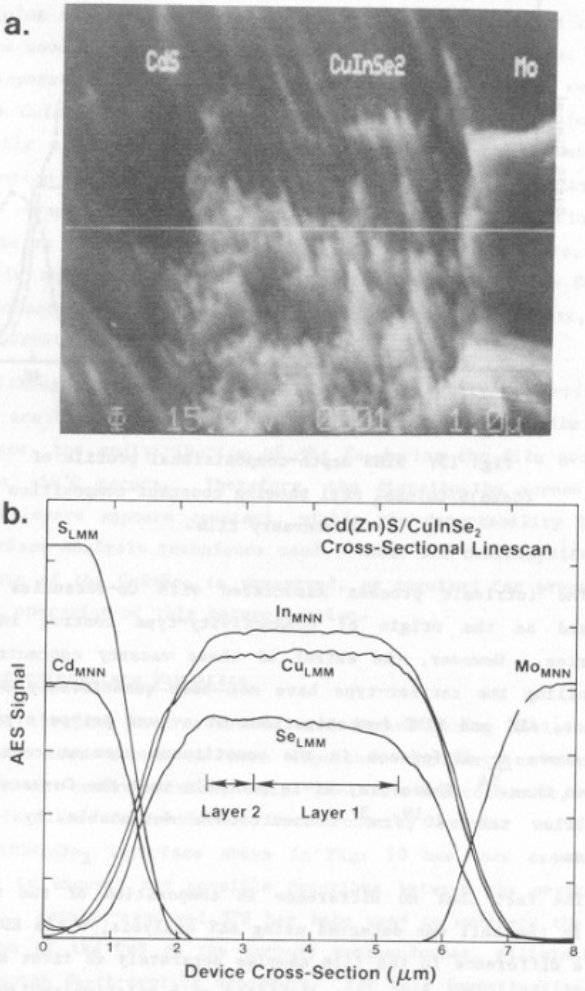

Fig. 12: $(CdZn)S/CuInSe_2$ thin-film solar cell: (a) Secondary electron micrograph of cell cross-section: (b) Scarning AES linescan indicating constant elemental compostion across Cu-ternary bilayer.

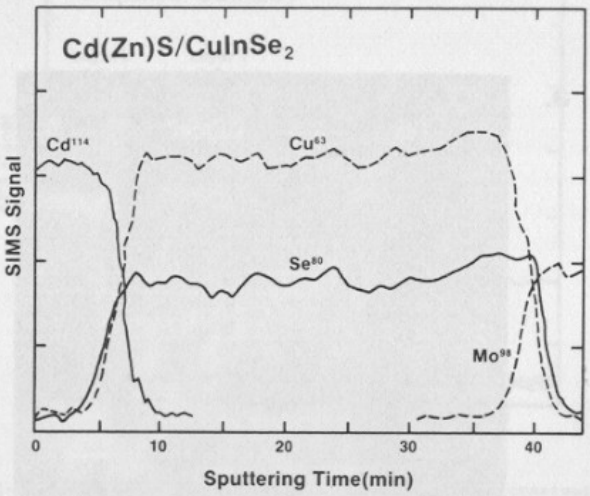

Fig. 13: SIMS depth-compositional profile of $(CdZn)S/CuInSe_2$ cell showing constant-composition Cu-ternary film.

The intrinsic process associated with Cu-vacancies has been proposed as the origin of conductivity-type control in the Cu-ternaries. However, the extent of these vacancy concentrations in controlling the carrier-type have not been quantifiably determined. In fact, AES and SIMS investigations of n- and p-type crystals have also shown no difference in the constituent element concentrations between them.[24] Therefore, it is probable that the Cu-vacancy levels are below the $\sim 10^{19}/cm^3$ concentration detectable by the Auger process.

The fact that no difference in composition of the two layers used in the cell was detected using AES analysis, while EDS did show such a difference in the film samples separately at first seems to be inconsistent. The films are deposited at a relatively-high substrate temperature (450°C). At this temperature, the diffusion coefficient of Cu (and other metals) in $CuInSe_2$ is relatively high.[25] Thus, the Cu tends to redistribute itself throughout the two layers, resulting

in a constant elemental composition. Evidence for this Cu-redistribution and diffusion process was provided in cells originally fabricated by a dual-source deposition method.[25] In this work, a source containing single-phase $CuInSe_2$ powder and another source containing Se were used to grow polycrystalline, p-type $CuInSe_2$ films. However, the evaporation of the ternary is not congruent. If the evaporation of the $CuInSe_2$ ws not carried to completion, a Cu-rich (containing primarily elemental Cu) portion of the evaporant was left in the evaporation source, and non-single phase thin films resulted. Only if the evaporation of the ternary was carred to completion was it possible to produce single-phase $CuInSe_2$ films. Therefore, the evidence is that at the substrate temperatures used for the Cu-ternary film formation, the Cu diffuses easily through the layers, and the proper crystal structure results.

Although large changes in the Cu:In substrate arrival rate ratios are used to vary the resistivity of the $CuInSe_2$ film near the interface, the redistribution of the Cu during the film growth process at 450°C occurs. Therefore, the distribution across the two ternary layers appears constant, within the detectability limits of the surface analysis techniques used. Thus, the chalcopyrite crystal structure of the $CuInSe_2$ is preserved, as required for proper photovoltaic operation of this heterojunction.

4.2 Heterointerface Formation

The chemical interaction between layers during device fabrication has been shown to have important implications for device behavior in heterojunction, metal-insulator-semiconductor, semiconductor-insulator-semiconductor, and Schottky barrier structures.[26] The CdS/$CuInSe_2$ interface shown in Fig. 10 has been examined more closely to uncover any possible reactions between the semiconductor species. Angular-resolved XPS has been used to evaluate the initial formation of the CdS on the ternary semiconductor, elliminating the sputter-etch depth-profile procedure. For this investigation, layers of CdS with approximately 20 Å- thickness steps were deposited over the $CuInSe_2$ substrate.[27] The sample had two CdS layers and an exposed $CuInSe_2$ section for analysis. The angular-resolved XPS data are presented in Fig. 14, showing the Cu-$2p_{1/2}$ and Cd-$3d_{5/8}$ signals

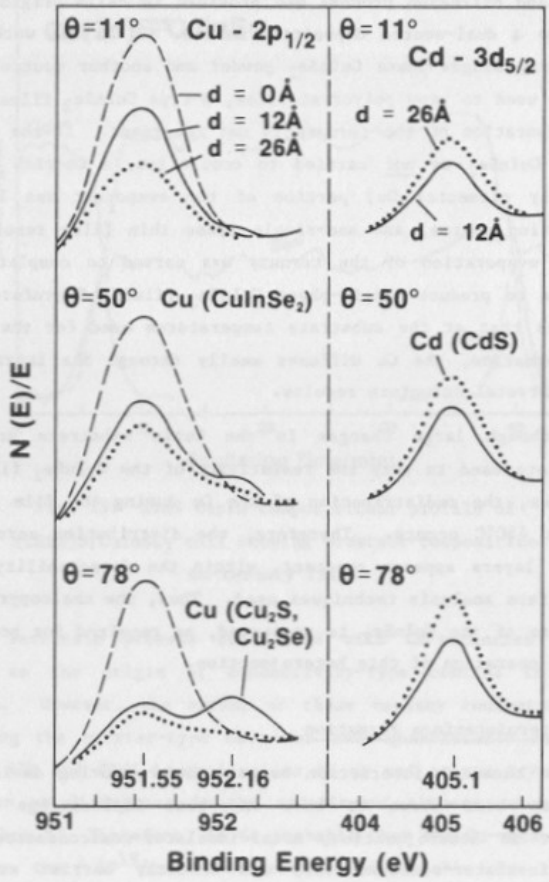

Fig. 14: Angular-resolved XPS data shaping Cu-$2p_{1/2}$ and Cd-$3d_{5/2}$ signals for various CdS thicknesses, d, on $CuInSe_2$. θ is analyzer acceptance angle (from ref. 21).

for various CdS thicknesses (d) and various acceptance angle (θ). The expected $Cu(CuInSe_2)$ XPS line at 951.55 eV is evident in all spectra. The additional line at 952.16 eV (as in the depth-profile case) emerges at high θ (the angle between the sample normal and the effective analyzer entrance), a condition of higher surface sensi-

tivity.[27] Once again, the line position indicates the presence of either Cu_2S or Cu_2Se of the XPS spectra has also shown both the Auger transitions corresponding to the : binary semiconductors. These angular-resolved data confirm the istence of the mixed-binary transition layer at the interface. The thickness of the transition layer can be estimated from these angular-resolved data and found to be in the range of 8-30 Å.[27]

The reaction between metal species and semiconductors has been investigated using electron energy loss spectr(copy (EELS), by employing this method to monitor changes in electronic e itations. Brillson has studied the initial stages of Schottky barrier formation using CdS and CdSe.[2] Reactions of Cu on these semiconductors have produced EELS spectra with features suggesting the formation of Cu_2S and Cu_2Se. In addition, the heats of reaction of this m tal with the compound semiconductors are favorable > Cu_2S and Cu_2Se formation.

EELS spectra for the formation of the CdS/$CuInSe_2$ interface are presented in Fig. 15. The spectrum for a clean (sputtered) $CuInSe_2$ substrate is shown in Fig. 15(c). The peak at 4.0 eV corresponds to he Cu-3d and In-5s. The Se-4p is at 5.6 eV and Se-4s, at 12.2 eV. The 17.4 peak is identified as the In-4d.[5] Interband transition and bulk and surface plasmons account for the remaining features.[29] After deposition of approximately 14 Å of CdS, the EELS spectrum shows a significant change. The spectrum is not completely that reported for CdS, although several interband transitions (e.g., 3.0 and 5.7 eV) and the Cd-4d (13.6 eV) and surface plasmon (10.6 eV) peaks are present. Features in the shaded region do not correspond to either CdS or $CuInSe_2$ spectra, indicating that some chemical interfacial reaction has occurred. In Fig. 15(c), the trend continues with some additional increase in the CdS EELS signals. However, the additional (reacted species) features are still observed. After a rather thick (300 Å) CdS film is deposited (Fig. 15(d)), the EELS spectrum is that expected for CdS. The EELS signals in the shaded regions of Fig. 15(b) and (c) are suggestive of the data for Cu on CdS reported by Brillson.[28] The aks at 8.8 and 11.2 eV correspond to his interpretation of the formation of Cu_2S at the Cu-CdS interface. These EELS data, therefore, complement the

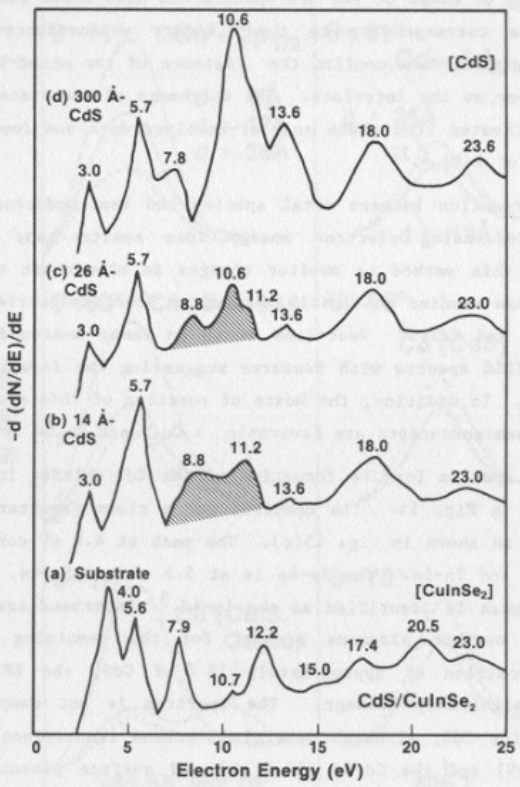

Fig. 15: EELS spectrum showing effects of growth of CdS film on $CuInSe_2$ substrate. Shaded regions indicate possible reacted species at interface (From ref. 21).

angular-resolved XPS measurement, and confirm the existence of a chemical reaction at the CdS-$CuInSe_2$ interface.[24] Furthermore, the resulting spectra again suggest that the reacted species are the Cu-binary compounds.

reported for CdS, although several interband transitions (e.g., 3.0 and 5.7 eV) and the Cd-4d (13.6 eV) and surface plasmon (10.6 eV) peaks are present. Features in the shaded region do not correspond to either CdS or $CuInSe_2$ spectra, indicating that some chemical interfacial reaction has occurred. In Fig. 15(c), the trend continues with some additional increase in the CdS EELS signals. However, the additional (reacted species) features are still observed. After a rather thick (300 Å) CdS film is deposited (Fig. 15(d)), the EELS spectrum is that expected for CdS. The EELS signals in the shaded regions of Fig. 15(b) and (c) are suggestive of the data for Cu on CdS reported by Brillson.[28] The peaks at 8.8 and 11.2 eV correspond to his interpretation of the formation of Cu_2S at the Cu-CdS interface. These EELS data, therefore, complement the angular-resolved XPS measurement, and confirm the existence of a chemical reaction at the CdS-$CuInSe_2$ interface.[24] Furthermore, the resulting spectra again suggest that the reacted species are the Cu-binary compounds.

4.3 Cell Heat Treatments

A major and critical step in the fabrication of high-efficiency CdS and Cd(Zn)S/$CuInSe_2$ heterojunction solar cells is the post-deposition heat-treatment.[21] However, significant improvement in device parameters is only observed when the annealing environment contains oxygen. The realtive improvement is illustrated in the light J-V characteristics of Fig. 16. Heating in high vacuum Ar, N, He, etc. does not seem to change cell performance substantially. Treatments (200 - 240°C) in oxygen (or air) consistently improve the operating characteristics.

Investigations of the back contact by Russell, et al.[30] using high resolution EBIC techniques provided some unexpected results. Both heat-treated and non heat-treated cells were fractured, and examined for electrical response across their cross sections. All devices show some activity at the back contact due to the Schottky barrier between the Mo and the $CuInSe_2$. Unheated cells, however, do not exhibit any uniform response at the heterojunction. It was initially proposed that the oxygen somehow caused the type-conversion of the Cu-ternary during the annealing process, improvement. C-V

4.3 Cell Heat Treatments

A major and critical step in the fabrication of high-efficiency CdS and Cd(Zn)S/$CuInSe_2$ heterojunction solar cells is the post-deposition heat-treatment.[21] However, significant improvement in device parameters is only observed when the annealing environment contains oxygen. The realtive improvement is illustrated in the light J-V characteristics of Fig. 16. Heating in high vacuum Ar, N, He, etc.

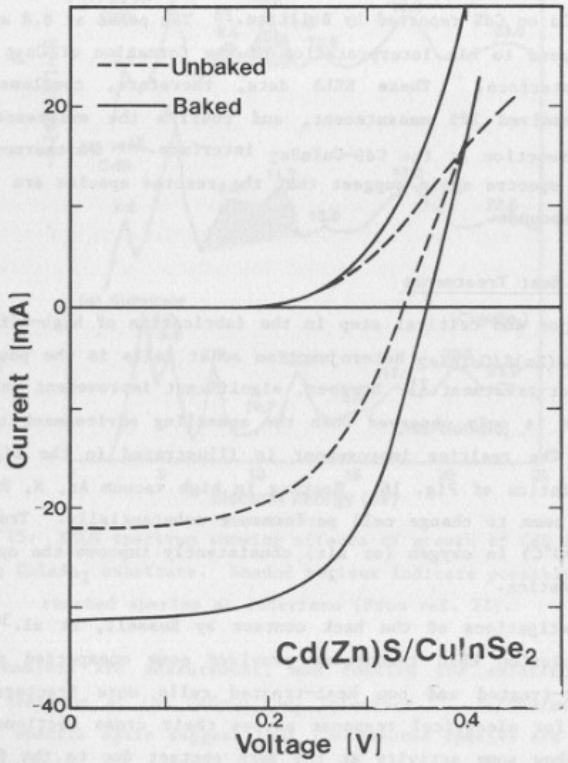

Fig. 16: Light current-voltage characteristics of (CdZn)S/$CuInSe_2$ solar cells: (a) unbaked; (b) baked in oxygen.

does not seem to change cell performance substantially Treatments (200 - 240°C) in oxygen (or air) consistently improve the operating characteristics.

Investigations of the back contact by Russell, et al.[30] using high resolution EBIC techniques provided some unexpected results. Both heat-treated and non heat-treated cells were fractured, and examined for electrical response across their cross sections. All devices show some activity at the back contact due to the Schottky barrier between the Mo and the $CuInSe_2$. Unheated cells, however, do not exhibit any uniform response at the heterojunction. It was initially proposed that the oxygen somehow caused the type-conversion of the Cu-ternary during the annealing process, improvement. C-V data have shown that n-type $CuInSe_2$ is in contact with the Mo in unbaked cells.[31] However, heat treatments in various environments have been shown to be effective in activating the EBIC response at the heterojunction, without any significant increase in cell efficiency. Such data is presented in Fig. 17 for a cell fractured

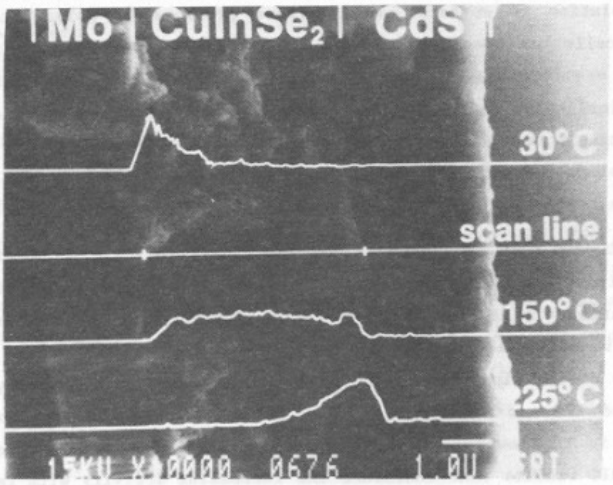

Fig. 17: EBIC linescan sequence as a function of in-situ, vacuum heat treatment, superimposed on secondary image of fractured cell cross-section (from ref. 31).

and heated in-situ in the vacuum environment of the analysis system. The EBIC data clearly show the activation of the heterojunction, and the decrease in response at the Schottky barrier. Complementary C-V data indicate the type-conversion of the Cu-ternary accompanying this process. This is likely due to the movement of Cu-vacancies--the only known source of p-type activity in $CuInSe_2$ -- to this region.

It should be emphasized that the oxygen is required to provide the significant increase in cell efficiency. However, its exact role is not known. SIMS data on the $CuInSe_2$ film taken before and after heat treatment in oxygen have shown no change in oxygen content in the films. (The background level in the Cu-ternary is about $10^{15}/cm^3$.) The oxygen does affect the CdS, lowering its resistivity. This could partially account for the change in cell performance, but more studies of the process are required.

5. Summary

The utility of high-resolution surface analysis in the detection and solution of surface and interface problems in polycrystalline solar cells has been demonstrated. The complementary application of these techniques, in conjunction with microelectrical characterization methods, has been utilized to investigate two photovoltaic device types.

- o polycrystalline Si:
- o (CdZn)S/$CuInSe_2$ heterojunction.

AES and SIMS were used to map impurities at grain boundaries in the polycrystalline Si. Minority carriers lifetime data showed some correlation with the impurity content. However, the major effect on grain boundary activation is the segregation of oxygen to these regions during high-temperature (> 650°C) processing. SIMS, angular-resolved XPS and EELS were used to directly detect the presence of oxygen in the boundaries. These compositional data were correlated with EBIC results that confirmed the increasing activity with temperature and oxygen content in the intergrain regions.

The interfaces in the Cu-ternary heterojunction were examined with several surface analysis techniques. The $CuInSe_2$ bilayer was shown to have uniform composition (within the 0.1 at-% detetion limit

of the AES method) due to the high diffusion coefficient of Cu, even at relatively low (450°C) deposition temperatures. SIMS data confirm these analyses. The initial formation of the heterojunction was studied using angular-resolved XPS. A mixed Cu_2S-Cu_2Se binary transition layer is found to exist at the interface between the CdS and the $CuInSe_2$. The effects of post-fabrication heat treatment on the junction activity in the device indicated that the major response is at the back contact before annealing, and shifts to the heterojunction after heating. Such heterojunction activation does not depend upon the ambient in which the device is heat treated. The exact effect(s) of the critical oxygen in the improvement of the device efficiency is not known. SIMS and AES analyses have shown no change in oxygen content of the Cu-ternary film after oxygen annealing. However, a lowering of the resistivity of the CdS layer is observed, and this could partially explain the change in performance. In the case of this solar cell, the application of surface analysis has not yet provided an explanation of device behavior, but has contributed to the process of eliminating several proposed mechanisms.

Acknowledgements

The author would like to thank and gratefully acknowledge P.J. Ireland, T.P. Massopust, R.K. Ahrenkiel, R. Matson, J. Dick, D. Cahen and O. Jamjoum of SERI who did many of the experimental studies. The cooperation of R.A. Mickelsen and W.S. Chen of Boeing Aerospace who supplied the devices is also appreciated. This work was performed by the Solar Energy Research Institute under Prime Contract EG-77-01-4042 to the U.S. Department of Energy. Finally, the author expresses his sincere appreciation to the Organization of American States and the Sociedade Brasileira de Vacuo for their support, and the cooperation of IME and SERI.

References

1. L.L. Kazmerski, Appl. Surf. Sci. 7 (1981) 55.
2. H. Windawi and F.F.L. Ho (Eds.) Applied Electron Spectroscopy for Chemical Analysis, J. Wiley and Sons, New York, 1982.

3. L.L. Kazmerski, Proc. SPIE (SPIE, Bellingham, Wash.; 1980) pp. 132-137.
4. D. Briggs, Handbook of X-ray and Photoelectron Spectroscopy, Heyden, London, 1978.
5. A.W. Czanderna, Ed., Methods of Surface Analysis, Elsevier Scientific, New York, 1975.
6. C.R. Brundle and A.D. Baker, Electron Spectroscopy: Theory, Techniques and Applications, Academic Press, New York, 1977-80 Vol. 1-3.
7. T.A. Carlson, Photoelectron and Auger Spectroscopy, Plenum Press, New York, 1975.
8 H.J. Leamy, in Physical Electron Microscopy, O.C. Wells, K.F.J. Heinrich and D.E. Newbury, Eds, Van Nostrand-Reinhold, New York, 1981.
9. L.L. Kazmerski, P.J. Ireland and T.F. Ciszek, Appl. Phys. Lett. 36 (1980) 323.
10. L.L. Kazmerski, J. Vac. Sci Technol. 20, 423 (1982).
11. L.L. Kazmerski and P.E. Russell, J. de Physique 43 (1983).
12. C.H. Seager, D.S. Ginley and J.D. Zook, Appl. Phys. Lett. 36, (1980) 831.
13. C.H. Seager, D.J. Sharp, J.K.G. Panitz and R.V. D'Aiello, J. Vac. Sci. Technol. 20 (1982) 430.
14. J.I. Pankove, M.A. Lampert and M.L. Targ, Appl. Phys. Lett. 32 (1978) 439.
15. G.C. Jain, B.C. Chakravarty and A. Prasad, J. Appl. Phys. 52 (1981) 3700.
16. D. Redfield, Appl. Phys. Lett. 38 (1981) 174.
17. M. Hirose, M. Taniquehi and Y. Osaka, J. Appl. Phys. 50 (1979) 377.
18. P.E. Russell and C.R. Herrington, D.E. Burke and P.H. Holloway, in Grain Boundaries in Semiconductors, North-Holland, New York, 1982, pp. 185-191.
19. J.C.C. Fan and L.L. Kazmerski, Proc. 16th IEEE Photovoltaic Spec. Conf. (IEEE, New York; 1983) pp. 2431-2446.
20. L.L. Kazmerski, Proc. 16th IECEC 2 (1981) 1637.
21. R.A. Mickelsen, W.S. Chen and L.F. Buldhaupt, Cadmium Sulfide/ Copper Ternary Cell Research, Final Report, XJ-9-8021-1, Boeing Aerospace, Seattle, 1982.

22. J.L. Shay and J.H. Wernick, Ternary Chalcopyrite Semiconductors; Growth Electronic Properties and Applications, Pergamon Press, New York, 1975, pp. 1-15, 175-214.

23. M. Prutton, L.A. Larsen and H. Poppa, J. Appl. Phys. 54 (1983) 374.

24. L.L. Kazmerski, T.P. Massopust, P.J. Ireland, O. Jamjoum, R.J. Matson, P.E. Russell, A. Hermann and J.R. Dick, Scanning Electron Microscopy/1983 (in press).

25. L.L. Kazmerski, in Ternary Compounds 1977, G.D. Holah, Ed., Institute of Phys., London, 1979, pp. 217-228.

26. See, for example, A.K. Sinha and J.M. Poate, in Thin Films: Interdiffusion and Reactions, J.M. Poate, K.N. Tu and J.W. Mayer, Eds., Wiley-Intersciences, New York, 1978, pp. 407-432.

27. L.L. Kazmerski, O. Jamjoum and P.J. Ireland, J. Appl. Phys. 54 (1983) 374.

28. L.J. Brillson, Phys. Rev. B18 (1978) 2431.

29. O. Jamjoum, L.L. Kazmerski, D.L. Lichtman and K.J. Bachmann, Surf. and Interface Anal. 4 (1982) 227.

30. P.E. Russell, O. Jamjoum, R.K. Ahrenkiel, L.L. Kazmerski, R.A. Mickelsen and W.S. Chen, Appl. Phys. Lett. 40 (1982) 995.

31. R.K. Ahrenkiel, L.L. Kazmerski, R.J. Matson, C.R. Osterwald, T.P. Massopust, R.A. Mickelsen and W.S. Chen, Appl. Phys. Lett. (in press).